Hindawi Publishing Corporation
Advances in Aerospace Engineering
Volume 2014, Article ID 847097, 17 pages
http://dx.doi.org/10.1155/2014/847097

Research Article

Global Modeling of CO_2 Discharges with Aerospace Applications

Chloe Berenguer and Konstantinos Katsonis

DEDALOS Ltd., Vassilissis Olgas 128, 54645 Thessaloniki, Greece

Correspondence should be addressed to Konstantinos Katsonis; katsonis.dedalos@gmail.com

Received 14 July 2014; Accepted 4 November 2014; Published 18 December 2014

Academic Editor: Martin Tajmar

We developed a global model aiming to study discharges in CO_2 under various conditions, pertaining to a large spectrum of pressure, absorbed energy, and feeding values. Various physical conditions and form factors have been investigated. The model was applied to a case of radiofrequency discharge and to helicon type devices functioning in low and high feed conditions. In general, main charged species were found to be ${CO_2}^+$ for sufficiently low pressure cases and O^- for higher pressure ones, followed by ${CO_2}^+$, CO^+, and ${O_2}^+$ in the latter case. Dominant reaction is dissociation of CO_2 resulting into CO production. Electronegativity, important for radiofrequency discharges, increases with pressure, arriving up to 3 for high flow rates for absorbed power of 250 W, and diminishes with increasing absorbed power. Model results pertaining to radiofrequency type plasma discharges are found in satisfactory agreement with those available from an existing experiment. Application to low and high flow rates feedings cases of helicon thruster allowed for evaluation of thruster functioning conditions pertaining to absorbed powers from 50 W to 1.8 kW. The model allows for a detailed evaluation of the CO_2 potential to be used as propellant in electric propulsion devices.

1. Introduction

Global Modeling (GM) has been lately extensively used for theoretical study of various types of plasma discharges in view of their applications. Reviews of GM applications including references to older publications can be found elsewhere; see, for example, [1, 2], for an extensive bibliography on the subject. GM allowed for successful investigation of plasmas of various compositions addressing natural conditions and specifically physical conditions and form factors with various applications in mind. In what concerns CO_2, to which focuses the present study, its presence in the atmosphere of Earth is of paramount importance for the environment [3], being a main greenhouse gas. Besides, CO_2 is a constituent of various atmospheres in the solar system planets and satellites [4–6]. Carbon oxides are also present in the composition of asteroids and comets [7]. Moreover, various laboratory and industrial applications call for the study of CO_2 plasmas, such as various types of plasma reactors. In this domain, we compare our theoretical results with experimental ones obtained in a radiofrequency discharge [3] meant to investigate the efficiency of CO_2 dissociation in view of reducing the CO_2 emissions. We also address here specifically Electric Propulsion (EP) applications using CO_2 as propellant, because of its important presence in various space environments. Noteworthy, EP devices dedicated to low Mars orbit satellites propulsion are of paramount importance in this context. Also, as was the case with previous GM studies [2, 8–10] the present GM of CO_2 discharges can be used as a basis of atmospheric entrance studies, notably in the case of Mars (typically 95% of CO_2 plus N_2 and Ar), provided the important hydrodynamic constraints are taken into consideration.

Functioning Diagrams (FD) and the corresponding Plasma Components Composition (PCC) diagrams which are obtained in the present study are important to monitor experimentally EP devices, mainly by optical emission spectroscopy and also theoretically by comparison with corresponding results (electron temperature T_e, line intensities) obtained from "zero-dimensional" collisional-radiative models. The latter are also useful for calculating the resonant vacuum ultraviolet (VUV) line intensities and so evaluate the radiative plasma cooling and the erosion of the plasma facing components in thrusters. With increasing absorbed energy and functioning time, erosion evaluation becomes particularly important.

In Section 2 of the present paper, the essentials of a GM are reported summarily, together with the necessary atomic

and molecular parameters, notably those used in the CO_2 case. Atomic and molecular data being of interest to our GM are specifically addressed. Description of the GM elaboration techniques is not reported here, as it is available elsewhere (see e.g., [1, 2, 11] and references therein). Also, sensitivity of the used parameters is not specifically investigated, because previous GM studies of various plasmas compositions showed in general a smooth variation [12]. In Section 3, theoretical results obtained from our model and general considerations concerning CO_2 discharges in higher pressures, pertaining to lower electron temperatures (T_e), are given and commented. They are compared in Section 4 with GM results obtained for plasmas of various compositions including mixtures with Ar and with the aforementioned experimental results for CO_2 from [3]. In Section 5, our GM results pertaining to lower pressures are given. They are of specific interest to EP because ionization is a key parameter for thrust. In general, these sufficiently ionized plasmas are characterized by quite high T_e. These results can be compared with previously obtained ones for EP applications using a common propellant such as Ar but also in case of feeding with N_2O, N_2, and O_2 and with mixtures of the two latter ones, hence with the air in various altitudes. An overview of such results is given in [2]. In Section 5 FDs giving the total ionization percentage ξ_{TOT} as a function of pressure p, for various absorbed power P_{abs} and T_e values and occasionally the corresponding PCCs, are presented for each EP case investigated. Concomitant T_e and ξ_{TOT} variations are also discussed in Section 5. Conclusions are given in Section 6.

2. GM Equations and CO_2 Atomic and Molecular Data

In this section, after giving a short description of the GM construction, necessary for the introduction of the basic definitions, we review the CO_2 atomic and molecular data which we had used in our model.

2.1. Summary Model Description. The GM is essentially composed of one power balance equation and of a system of particle balance equations [10]. The power balance equation, giving the power dependence of the electron density, can be written in a condensed form as follows:

$$\frac{P_{abs}}{V} = \sum_X e\varepsilon_{C,X} k_{IONIZ,X} n_X n_e + \sum_{X+} e\left(\varepsilon_e + \varepsilon_i\right) k_{RW,X+} n_{X+} \tag{1}$$

X represents here each of the main Ground Level (GL) species, with $k_{IONIZ,X}$ and $k_{RW,X+}$ the corresponding ionization rate and the wall recombination rate. The total energy loss $\varepsilon_{T,X} = \varepsilon_e + \varepsilon_i + \varepsilon_{C,X}$ is essentially composed of three terms, ε_e and ε_i being the mean kinetic energy lost per electron and per ion, respectively, and $\varepsilon_{C,X}$ the energy lost to collisions of electrons with heavy particles X. All $\varepsilon_{C,X}$ have to be calculated for the main considered heavy particles X, namely, CO_2, CO, O, and O_2. Moreover, V represents the plasma volume and n_e and n_X are the densities of electrons and of the species X, respectively, as usually. The area for effective loss A_{eff} included in the term k_{RW} of (1) is given by $A_{eff} = 2\pi(h_L R^2 + h_R RL)$ with R and L the radius and length of the plasma and h_L and h_R the axial and radial edge to center ratios of positive ion density. These are modified Godyak factors that can be extended to high pressure, as derived in [13] or to electronegative discharges [14]. The plasma sheath depends strongly on the Bohm velocity u_B, which for CO_2 is $u_{B,CO_2^+} = (eT_e/M_{CO_2})^{1/2}$, where e is the electron charge and M_{CO_2} is the mass of the CO_2 molecule. An example of sheath calculation has been given in [10]. For the plasma reactor case, we use a combined cross section value of 285 Å^2 for the ionic momentum transfer corresponding to an ionic sheath composition of 40% CO_2^+, 40% of CO^+, and 20% of O_2^+.

Each of the particle balance equations is constituted by the sum of all the creation and destruction terms for a given species j and can be written:

$$\frac{dn_j}{dt} = \sum R^j_{\text{Production}} - \sum R^j_{\text{Loss}}, \tag{2}$$

where $\sum$ denotes the sum of all $R^j_{\text{Production}}$ and R^j_{Loss} terms. For an equation pertaining to j, each term includes production or loss rates involving the species j. Production and loss reaction rates are given by the product of the reactant densities n_i with the corresponding rate coefficient k_j:

$$R^j = k_j \cdot \prod_i n_i \quad \left(\text{cm}^{-3}\,\text{s}^{-1}\right). \tag{3}$$

2.2. Atomic and Molecular Data Description. A list of the considered CO_2 states with their energies is given in Table 1. Inelastic reactions considered in the model are given in Tables 2 to 4 including occasionally references where they have been previously reported. Table 1, containing structure data of CO_2, includes the energies of the excited states, both electronic and vibrational. Excitation of all those states is taken into account by the collisional energy loss term ε_{C,CO_2}. The character of each electronic transition, allowed or forbidden, is indicated following [15]. Energy values were taken from [16, 17] and excitation cross sections used in ε_{C,CO_2} from [15, 16]. The list of the 20 processes included in the GM, involving the CO_2 and CO species and their ions, is given in Table 2. Note that CO_2 elastic scattering rate is introduced only in the power balance equation under ε_{C,CO_2} in order to determine the entirety of energy losses, including those coming from various types of GL excitation, dissociation, and ionization. Reaction rates are separately included in the respective particle balance equations and participate in the determination of the populations provided by the set of the statistical equations. Table 3 gives the list of the 20 processes involving oxygen species included in the GM. Processes involving carbon species are contained in Table 4.

Table 3 constitutes an extended version of Table 4 appearing in [12]. No source is given for cross sections/rate coefficients for which references are available in [12]. Moreover, reference [17] contains an extended list of related references. It has to be noted that C_2 formation on the wall has been neglected in the present status of the model. Rates for

Table 1: Structure description of the states of CO_2 as included in the GM.

i	Configuration	Energy (eV)	Type	Excitation energy sources	Excitation cross sections sources
1	^3X	0.			
2	^3X (010)	0.083		[16, 17]	a, b in [16]
3	^3X (100)	0.172		[16, 17]	b, c in [16]
4	^3X (001)	0.29		[16, 17]	a, b in [16]
5	$^3\sum_u$	8.15	Forbidden	d in [16]	e in [15]
6	$^3\prod_g$	8.73	Forbidden	d in [16]	e in [15]
7	$^3\Delta_u$	8.80	Forbidden	d in [16]	e in [15]
8	$^1\prod_g$	8.93	Allowed	d in [16]	e in [15]
9	$^1\Delta_u$	9.32	Allowed	d in [16]	e in [15]
10	$^1\sum_u{}^+$	11.00	Allowed	d in [16]	e in [15]
11	$^3\prod_u$	11.31	Forbidden	d in [16]	e in [15]
12	$^1\prod_u$	11.39	Allowed	d in [16]	e in [15]

a: Nakamura [18]; b: Kitajima et al. [19]; c: Kochem et al. [20]; d: Nakatsuji [21] as reported in [16]; e: extrapolated in the low energy region following the Quasi-Classical approximation.

Table 2: Reactions involving CO_2, $CO_2{}^+$, CO, and CO^+ species considered in the CO_2/CO plasma kinetics.

Number	Process		Description	Source for the cross section/rate coefficient
1	$CO_2 + e^- \rightarrow CO_2{}^+ + 2e^-$	(I)	CO_2 ionization	f in [16]
2	$CO_2(v = 0) + e^- \leftrightarrow CO_2(v) + e^-$	(II)	CO_2 vib. (de-)excitation	a, b, c in [16], see Table 1
3	$CO_2 + e^- \rightarrow O^+ + CO + 2e^-$		CO_2 dissociative ionization	f in [16]
4	$CO_2 + e^- \rightarrow CO^+ + O + 2e^-$		CO_2 dissociative ionization	f in [16]
5	$CO_2{}^+{}_{wall} \rightarrow CO_2$		$CO_2{}^+$ wall recombination	Formula (4), from [22]
6	$CO_2 + e^- \rightarrow CO + O(^1D) + e^-$	(III)	CO_2 dissociation	g in [16]
7	$CO_2 + e^- \rightarrow CO + O(^3P) + e^-$		CO_2 dissociation	Evaluation, present work
8	$CO_2 + e^- \rightarrow CO + O^-$	(IV)	CO_2 dissociative attachment	h in [16]
9	$CO_2{}^+ + O^- \rightarrow CO_2 + O$		$CO_2{}^+$ recombination with O^-	Evaluation, present work
10	$CO_2{}^+ + e^- \rightarrow CO + O$	(V)	$CO_2{}^+$ diss. recombination	i in [4]
11	$CO + e^- \rightarrow CO^+ + 2e^-$		CO ionization	[17]
12	$CO + e^- \rightarrow C^+ + O + 2e^-$		CO dissociative ionization	[17]
13	$CO + e^- \rightarrow C + O^+ + 2e^-$		CO dissociative ionization	[17]
14	$CO + e^- \rightarrow C + O^- + e^-$		CO dissociative attachment	[17]
15	$CO^+{}_{wall} \rightarrow CO$		CO^+ wall recombination	Formula (4), from [22]
16	$CO^+ + e^- \rightarrow C + O$		$CO_2{}^+$ diss. recombination	Evaluation, present work
17	$CO^+ + O^- \rightarrow CO + O$		$CO_2{}^+$ recombination with O^-	Evaluation, present work
18	$CO + O(^1D) \rightarrow CO + O(^3P)$		$O(^1D)$ de-excitation with CO	Evaluation, present work
19	$CO_2 + O(^1D) \rightarrow CO + O_2$		CO_2 dissociation with $O(^1D)$	j in [23]
20	$CO + O(^1D) \rightarrow CO_2$		CO_2 form. from $O(^1D)$ + CO	Evaluation, present work

f: Lindsay and Mangan [24]; g: LeClair and McConkey [25]; h: Rapp and Briglia [26] as reported in [16]; i: Seiersen et al. [27] as reported in [4]; j: Sedlacek et al. [28] as reported in [23].
(I) Ionization rates from vibrationally excited levels of CO_2, based on values for ionization from $CO_2(v = 0)$ multiplied by a factor of 1.5.
(II) Vibrational (de-)excitation for v 001, 010, and 100 values.
(III) Using the rate for CO_2 dissociation leading to the $O(^1S)$ products.
(IV) The CO_2 dissociative attachment rate from vibrationally excited levels is based on values for ionization from $CO_2(v = 0)$ multiplied by a factor of 1.5.
(V) We used rate coefficient reported in [4] divided by a factor of 3.

reactions listed in Tables 1 to 4 were obtained by integration of cross sections, when the latter are available.

Excitation, dissociation, and ionization rates entering in (1) and (2) have been separately calculated and/or evaluated using our standard computer codes and also available measurements. To obtain the rate coefficients introduced in our GM, the evaluated cross sections have been integrated from threshold up to around 500 eV over a Maxwellian distribution. In doing so, available elastic collision cross sections have been interpolated for higher collision energies. Rate coefficients have been parameterized with algebraic polynomials and are all valid in the range 0.1 to 100 eV, following standard procedures detailed in [29]. Occasionally, these are noted by indexes corresponding to the process

Table 3: Reactions involving oxygen species considered in the CO_2 plasma kinetics.

*P*Number	Process		Description	Source
1	$O + e^- \rightarrow O^+ + 2e^-$		O ionization	
2	$O^+{}_{wall} \rightarrow O$		O^+ wall recombination	Formula (4), from [22]
3	$O_{wall} \rightarrow (1/2)\, O_2$		O_2 wall formation	Formula (5), from [22]
4	$O_2 + e^- \rightarrow O_2{}^+ + 2e^-$		O_2 ionization	
5	$O_2(v = 0) + e^- \leftrightarrow CO_2(v) + e^-$	(VI)	O_2 vib. (de-)excitation	
6	$O_2{}^+{}_{wall} \rightarrow O_2$		$O_2{}^+$ wall recombination	Formula (4), from [22]
7	$O_2{}^+ + e^- \rightarrow O + O$		$O_2{}^+$ diss. recombination	[31]
8	$O_2 + e^- \rightarrow 2O(^3P) + e^-$		O_2 dissociation	
9	$O_2 + e^- \rightarrow O(^3P) + O(^1D) + e^-$		O_2 dissociation	
10	$O(^1D)_{wall} \rightarrow O(^3P)$		$O(^1D)$ wall deexcitation	Formula (5), from [22]
11	$O(^3P) + e^- \leftrightarrow O(^1D) + e^-$		$O(^1D)$ excitation/deexc.	
12	$O(^1D)_{wall} \rightarrow (1/2)\, O_2$		O_2 wall formation	Formula (5), from [22]
13	$O(^1D) + e^- \rightarrow O^+ + 2e^-$		$O(^1D)$ ionization	
14	$O_2 + e^- \rightarrow O^- + O + e^-$		O_2 diss. attachment	
15	$O_2 + e^- \rightarrow O^- + O^+ + e^-$		O_2 dissocitative ionization	
16	$O_2 + e^- \rightarrow O + O^+ + 2e^-$		O_2 dissocitative ionization	
17	$O^+ + O^- \rightarrow 2O$		O^+ recombination with O^-	
18	$O_2{}^+ + O^- \rightarrow O_2 + O$		$O_2{}^+$ recombination with O^-	
19	$O + O^- \rightarrow O_2 + e^-$		O^- recombination with O	[32]
20	$O^+ + O_2 \rightarrow O + O_2{}^+$		$O^+/O_2{}^+$ charge exchange	[33]

(VI) Vibrational (de-)excitation for $v = 1$ and $v = 2$ values.

Table 4: Reactions involving carbon species considered in the CO_2 plasma kinetics.

P number	Process	Description	Source
1	$CO_2 + e^- \rightarrow C^+ + 2O + 2e^-$	CO_2 diss. ionization	f in [16]
2	$C^+{}_{wall} \rightarrow C$	C^+ wall recombination	Formula (4), from [22]
3	$C + e^- \rightarrow C^+ + 2e^-$	C ionization	[34]
4	$C^+ + CO \rightarrow C + CO^+$	C^+/CO^+ charge exchange	Evaluation, present work
5	$C^+ + O^- \rightarrow C + O$	$CO_2{}^+$ recombination	Evaluation, present work

f: Lindsay and Mangan [24], as reported in [16].

(IONIZ, RW, ...) or to the state $(X, X^+, \ldots)$, as is the case in (1). Collisions involving the wall (wall recombination RW, $X+$ and deexcitation DXW, j) have rates described by the formulas proposed in [22]:

$$k_{\mathrm{RW},X+} = \frac{u_{B,X+} \cdot A_{\mathrm{eff}}}{V} \quad \left(\mathrm{s}^{-1}\right), \tag{4}$$

$$k_{\mathrm{DXW},j} = \left[\frac{\Lambda^2}{D_j} + \frac{2V\left(2-\gamma_j\right)}{A_{\mathrm{eff}} v_j \gamma_j}\right]^{-1} \quad \left(\mathrm{s}^{-1}\right) \tag{5}$$

with $\Lambda^{-2} = (\pi/L)^2 + (2.405/R)^2$ the effective diffusion length and D_j the neutral diffusion coefficient of excited species j. The latter is given by $D_j = (k_B T_{\mathrm{GAS}} \lambda_j)/(v_j M_j)$, where k_B represents the Boltzmann constant and T_{GAS} is the gas temperature. The mean free path for collisions between two neutral species is $\lambda_j = 1/n_j \sigma_{j,X}$, where $\sigma_{j,X}$ is the cross section pertaining to state j of the one species with the other species X. Moreover, v_j is the neutrals mean velocity $v_j = (8k_B T_{\mathrm{GAS}}/\pi M_j)^{1/2}$ and γ_j is the sticking coefficient for the excited species j on the wall surface. For $CO_2(v)$ and for $O_2(v)$ we used here $\gamma = 0.5$. For O_2 formation on the wall, we also use (5) but conveniently adapted to the considered O species, with sticking parameter value $\gamma_O = 0.17$. This value has been previously proposed for stainless steel by [30].

2.3. Energy Losses from Electron Collisions in Low Ionization Cases. Determining the total collisional energy losses per electron-ion pair created is an important part of the development of a GM. It is essential for the power balance equation formulation, relating the electron density n_e to the input power as a function of the plasma constituents and of their energy losses due to collisions with electrons as a function of T_e. For each atomic or molecular species, energy is mainly lost by elastic scattering (ELAS), ionization (IONIZ), electronic excitation (EXC), vibrational excitation (VIB), and dissociation (DISS) processes, noted by the corresponding indexes as previously. These abbreviations are also used occasionally in the figures.

Whenever the ionization percentage is low (e.g., as in plasma reactors with ionization of about 1% or less), with T_e not too high, the energy losses due to ions can be neglected.

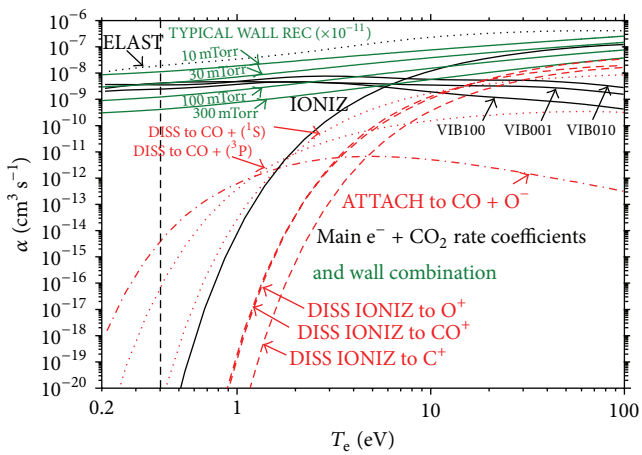

Figure 1: Main rate coefficients in CO_2 discharges; ELAST, REC, DISS, IONIZ, VIB, and ATTACH stand for elastic, recombination, dissociation, ionization, vibrational, and attachment, respectively. The α symbol on the vertical axis title stands here exceptionally for the rate coefficients; it is also noted k_j through the text.

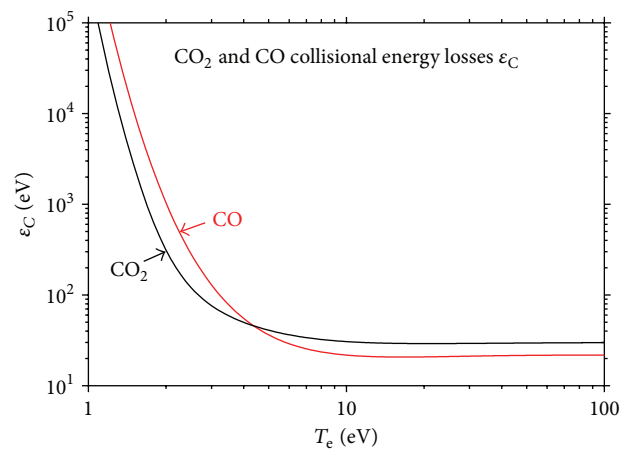

Figure 2: Electron collision energy losses for CO_2 and CO.

In this case, evaluation of the collisional energy losses, noted here ε_{C,CO_2}, is based on the following equation:

$$\varepsilon_{C,CO_2} = E_{IONIZ,CO_2} + E_{ELAS,CO_2}\frac{k_{ELAS,CO_2}}{k_{IONIZ,CO_2}} + \sum_i E_{VIB,CO_2,i}\frac{k_{VIB,CO_2,i}}{k_{IONIZ,CO_2}} + \sum_j E_{EXC,CO_2,j}\frac{k_{EXC,CO_2,j}}{k_{IONIZ,CO_2}} + \sum_k E_{DISS,CO_2,k}\frac{k_{DISS,CO_2,k}}{k_{IONIZ,CO_2}} \quad (6)$$

involving specifically CO_2. The ε_{C,CO_2} values, which we obtained, and consequently the electron density calculated by the GM are also here very sensitive on the values of the ionization cross sections, hence on the rate coefficients introduced in the collisional energy losses calculation. An equation similar to (6) exists, valid for $\varepsilon_{C,CO}$ parameter.

In case of plasma reactors functioning in inductively coupled plasma mode, most of the created ions are expected to recombine on the metallic wall and in view of the absorbed power the ionization percentage does not usually exceed 1%. In such conditions, given the also low percentage of the excited states population, the energy is practically lost by electron collisions with neutral ground level particles e^-–CO_2, e^-–CO, e^-–O_2, e^-–O through elastic, ionization, and excitation processes. As populations of carbon species are expected to be quite smaller, losses by ionizing e^-–C collisions have not been taken into account. This is also the case for the ionized species collisions, of which densities are often orders of magnitude smaller.

The main rate coefficients concerning CO_2, which we have used in the present GM, are shown in Figure 1 in order to ease the comparison of their relative importance.

The general properties of the electron collisional energy loss parameter are very important in determining where the absorbed energy is spent. Omitting significant components from the set of collisional processes entering in the model pattern may result to a considerable lowering of the corresponding electron collisional energy loss parameter values. In principle, values corresponding to molecules are much higher than those of C, O, and Ar plasmas of low T_e containing less than 1% of atoms, due to the presence of extravibrational states.

We evaluated the collisional energy losses of the CO_2, CO, O_2, and O that are of interest here mostly on the basis of cross sections coming from the literature. Especially for the last two species, see [2] and references therein. References pertaining to CO_2 have been given previously. Especially for CO, main references providing cross sections used for evaluation are [35–37] besides [17]. Elastic collision cross sections are very similar in CO_2 and CO. The obtained electron collisional energy loss parameters for both of them are given in Figure 2 (black curve for CO_2 and red one for CO) in the region of about 1 eV to 100 eV. The values become comparable in the region of about four eV.

3. Theoretical Results Pertaining to Pressure and Power Variations

We present and discuss GM results obtained for CO_2 discharges in a large region of pressures, typically from 1 mTorr to 1 Torr. We evaluate the plasma constituents densities, the T_e, the remaining CO_2 percentage, and the total ionization percentage ξ_{TOT} for a typical discharge form factor of L = 30.0 cm and R = 8.0 cm. These dimensions are practically the same as those of the experiment reported in [3]. The model could in principle give valid results even for higher pressures, provided that the number of terms in the power balance equation is extended to encompass more vibrational states of CO_2, CO, and O_2 molecules and their reactions and that the number of the particle balance equations is increased

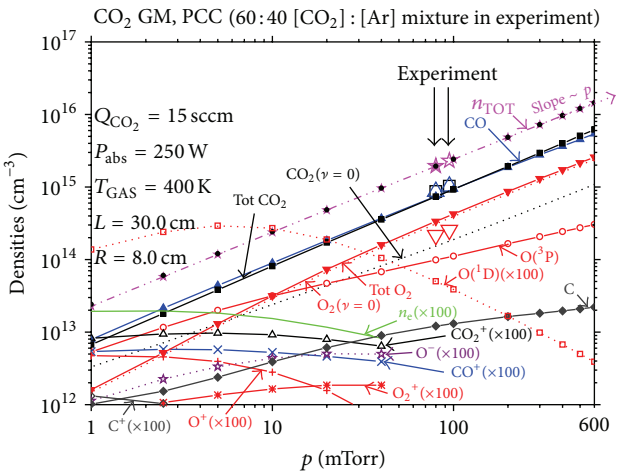

Figure 3: PCC for a feeding of 15 sccm and P_{abs} 250 W; Tot stands for total and EXPER for experiment.

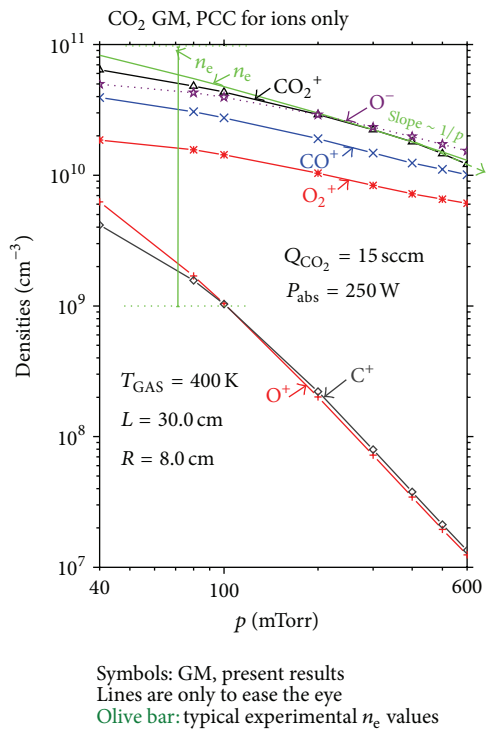

Figure 4: PCC for the same conditions than those of Figure 3 but for low densities and high pressures.

accordingly. Consideration of additional reactions could be also necessary in this case.

Investigating the plasma properties in the aforementioned pressure region, we first consider a typical absorbed power of 250 W; the obtained results are presented in Section 3.1. Although the conditions choices leading to results presented in this section are suggested by existing experimental results [3], results of the GM obtained for other absorbed power values have also been investigated. They were found to give analogous, smoothly varying results. Two feedings of 15 sccm and of 100 sccm are addressed in the present section, with plasma characteristics showing also smooth variations throughout.

Results pertaining to various absorbed power P_{abs} values were evaluated. These are presented and discussed in Section 3.2 for P_{abs} values going from 25 W up to 1 kW. Experimental results from [3], appearing in the quasitotality of Section 3 figures, noted by big symbols, will be separately discussed and compared with our results in Section 4.

3.1. Discharge Characteristics as a Function of the Pressure for 250 W of Absorbed Power. We assume here a gas temperature $T_{GAS} = 400$ K. Results pertaining to a lower feeding of 15 sccm are shown in Figures 3 to 5.

Density values for n_e and ionic species are shown in the bottom of Figure 3 multiplied by 100. Those pertaining to values of $p > 40$ mTorr, not shown in order to simplify the figure, are given in Figure 4. The obtained total plasma density and densities of CO_2, CO, O_2, and O and of their ions are shown for a low feeding of 15 sccm. Results of calculations of the two O atom ground levels (GL), $O(^3P)$ and $O(^1D)$, densities are given separately. Also, $\nu = 0$ indicates population densities of ground vibrational levels and the prefix Tot shows total density values. We see in Figure 3 that CO is slightly more present in the discharge than the total CO_2 (Tot CO_2) for low pressures. The inverse is true for high pressures, say after 100 mTorr. Densities of the GLs of atomic oxygen are higher than those of O_2 for lower pressures, where the latter is more easily dissociated, while for higher pressures O_2 density becomes an order of magnitude higher than the $O(^3P)$ GL one. The $O(^1D)$ densities, being much smaller than those of $O(^3P)$, are shown multiplied by 100. The presence of C in the discharge is lower than this of O, down to an order of magnitude for high pressures. High pressure densities of neutral components are varying following approximately a slope of $p/k_B \cdot T_{GAS}$. The plasma is low ionized, with the ion densities strongly diminishing after 100 mTorr and tending to a slope around $1/n_{TOT}$, where n_{TOT} represents the total density including all species.

The low ionized species densities are shown separately in Figure 4 in the 40 mTorr to 600 mTorr pressure region. Densities of positive ions CO_2^+, CO^+, and O_2^+ diminish to a rather similar way with increasing pressure. However, O^- density leading to electronegativity bypasses this of CO_2^+ after 200 mTorr. O^+ and C^+ densities become negligible. Figures 3 and 4 illustrate the continuous diminishing of the electron density n_e.

As is shown in Figure 5, when the pressure increases from 1 mTorr to 1 Torr, T_e is falling from about 4.4 eV to about 1.2 eV while the remaining CO_2 amount increases slowly, beginning from 28% for low pressures before stabilizing to about 43%. The quotient of the total O atoms to this of C atoms remains evidently equal to 2.

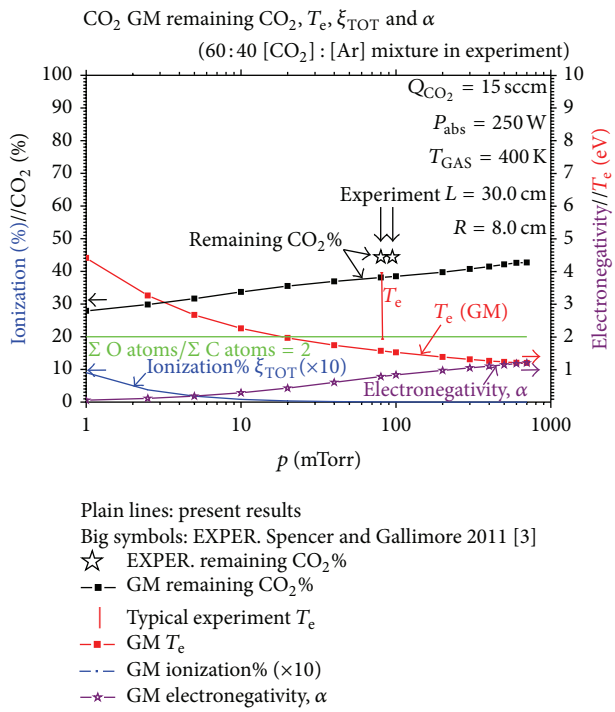

FIGURE 5: Remaining CO_2, T_e, ξ_{TOT}, and α as a function of the pressure for conditions of Figures 3 and 4; EXPER stands for experiment.

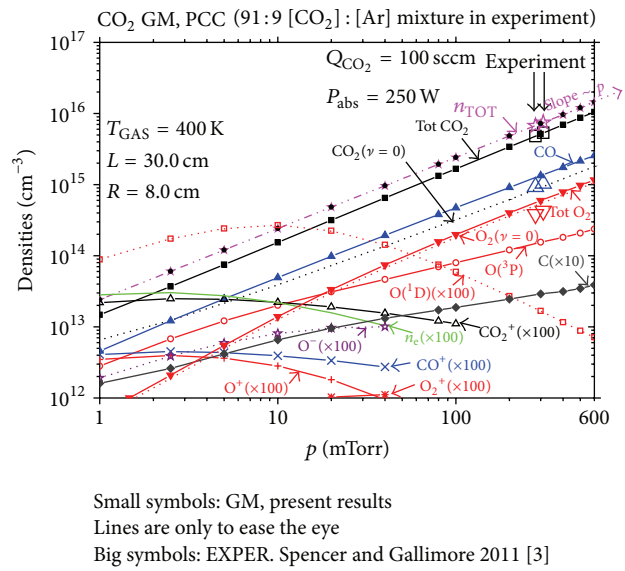

FIGURE 6: PCC for conditions similar to those of Figure 3 but for 100 sccm feeding; Tot stands for total and EXPER for experiment.

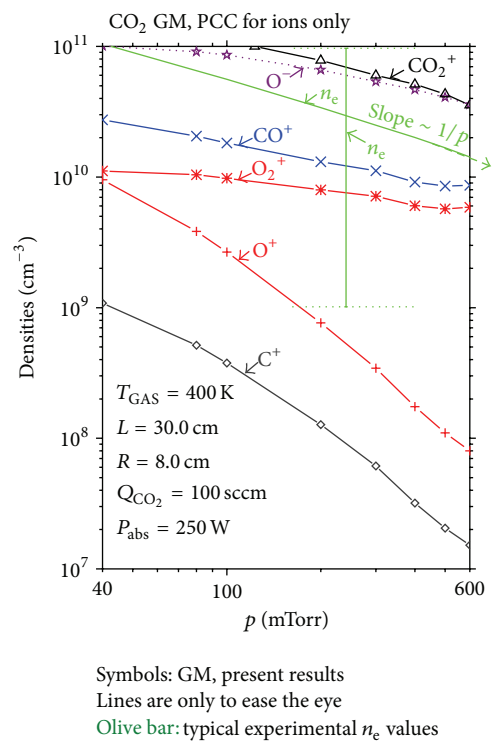

FIGURE 7: PCC for conditions similar to those of Figure 4 but for 100 sccm feeding.

While our results for a 15 sccm feeding indicate a percentage of the remaining CO_2 stabilizing to about 43%, this corresponding to a higher feed of 100 sccm shows the same tendency but leading to a higher percentage, of 73% approximately. Obviously, the absorbed power of 250 W considered in both cases while being able to dissociate more than half of CO_2 for the low feeding is not sufficient to dissociate much more than a quarter of the provided CO_2 when the feeding increases to 100 sccm.

Results pertaining specifically to a higher feeding of 100 sccm are shown in Figures 6 to 8. In Figure 6, similar to Figure 3 but for a high feeding, the total plasma density and densities of CO_2, CO, O_2, and C and of their ions together with $O(^3P)$ and $O(^1D)$ values are also given as a function of the pressure. Density values for n_e and ionic species are shown in the bottom of Figure 6 multiplied by 100. Except for CO_2^+, values for ionic species pertaining to values of $p > 40$ mTorr, not shown in order to simplify the figure, are given in the next Figure 7. We see that here CO is less present than Tot CO_2 in the discharge, followed by O_2. For lower pressures, densities of the atomic oxygen GLs are clearly higher than this of O_2, where the latter is more easily dissociated, while for higher pressures, O_2 density is almost an order of magnitude higher than the atomic oxygen one. Here also, densities of neutrals vary approximately according to a slope of $p/k_B \cdot T_{GAS}$. The plasma is low ionized, with the ion densities diminishing after 100 mTorr following a slope proportional to $1/n_{TOT}$.

As was the case in Figure 4, pertaining to a 15 sccm feeding, we show separately in Figure 7 our ion densities results for high pressures (40 mTorr to 600 mTorr). Variations are analogous to those shown in Figure 4 but with O^+ being quite more abundant than C^+, with differences being up to one order of magnitude for low pressures.

We show in Figure 8 that, with increasing pressure, T_e is falling from about 4.2 eV to about 1.3 eV as was the case with 15 sccm feeding, while the remaining CO_2 amount starts from

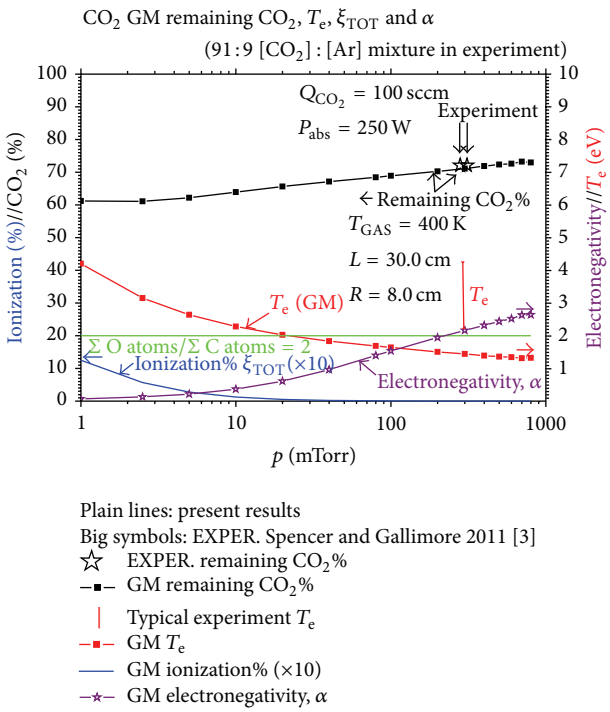

FIGURE 8: Remaining CO_2, T_e, ξ_{TOT}, and α as a function of the pressure for conditions of Figures 6 and 7; EXPER stands for experiment.

61% for 1 mTorr and becomes 73% for 1 Torr, quite different than in the 15 sccm case, shown in Figure 5.

3.2. Influence of the Absorbed Power. It is also interesting to know for a given feeding how the discharge properties vary with P_{abs}, when the pressure is kept constant. Typical results obtained for the low feeding of 15 sccm addressed previously are illustrated in Figures 9 to 11 for a pressure of 80 mTorr. Results are calculated for absorbed power values varying from 80 W to 1000 W and are illustrated by small symbols, joined by lines to ease the eye. For the sake of simplicity, only neutral species densities values are shown in Figure 9. Those of ionic species are given separately in Figure 10. Note that no symbols are included to mark the n_e and ionization percentage ξ_{TOT} values in the corresponding curves. Experimental values from [3] illustrated in Figures 9 to 14 by big symbols will be discussed in the next section, where experimental results for various gases pressures and mixtures will be also addressed.

Figure 9 shows a PCC as a function of the absorbed power P_{abs} for a n_{TOT} value of $2 \cdot 10^{15}$ cm^{-3}. Main components are total CO_2 (Tot CO_2) and CO with the latter starting evidently from lower density values than the former but arriving to about double values for 1 kW of absorbed power. O_2 densities increase slightly both for Tot O_2 and for vibrational state $\nu = 0$. $O(^3P)$ density, an order of magnitude lower than this of Tot CO_2, increases with absorbed power and finally exceeds this of Tot O_2. $O(^1D)$ density is roughly two orders of magnitude smaller. The C density is one order of magnitude lower that

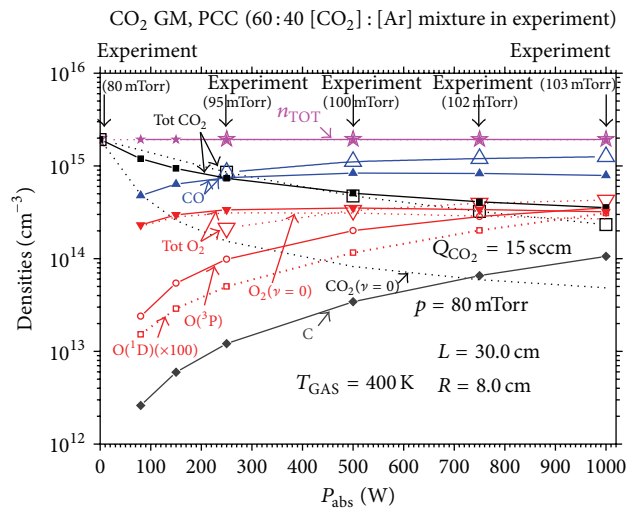

FIGURE 9: PCC as a function of the absorbed power P_{abs}; Tot stands for total and EXPER for experiment.

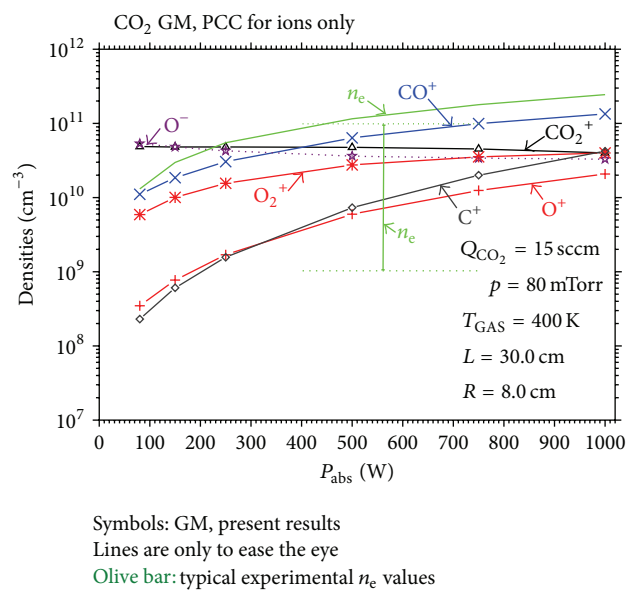

FIGURE 10: Low densities part of PCC showing ionic components.

the density of $O(^3P)$ for an absorbed power of 80 W, the difference diminishing for high absorbed powers.

Ionized components are separately shown in Figure 10 and have quite low densities. Densities of CO^+, O_2^+, C^+, and O^+ components presented in Figure 10 start from low values for 80 W and increase with absorbed power. Inspection of Figure 10 shows that with increasing absorbed power the O^- and CO_2^+ densities remain about the same, although slightly diminishing, while CO^+ and O_2^+ densities increase considerably. Densities of singly ionized positive atomic species (C^+, O^+) start from very low densities for low P_{abs} but increase with P_{abs} considerably, much faster than

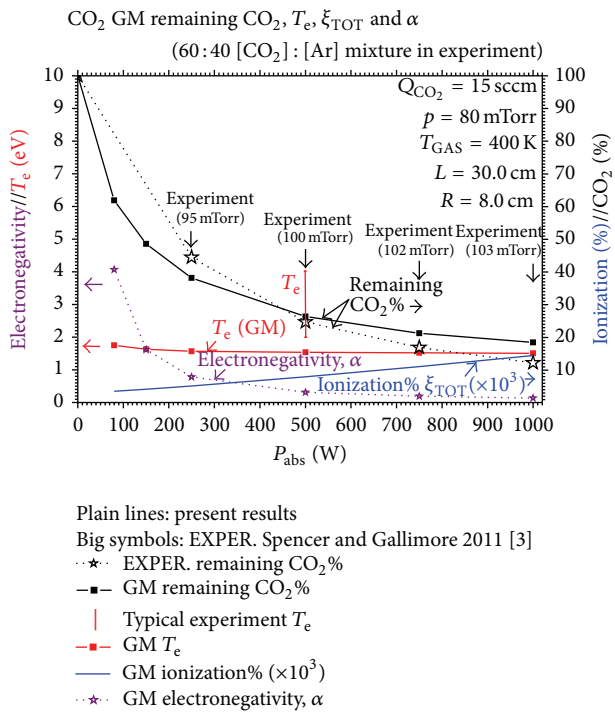

FIGURE 11: Remaining CO_2, T_e, ξ_{TOT}, and α as a function of the absorbed power P_{abs}; EXPER stands for experiment.

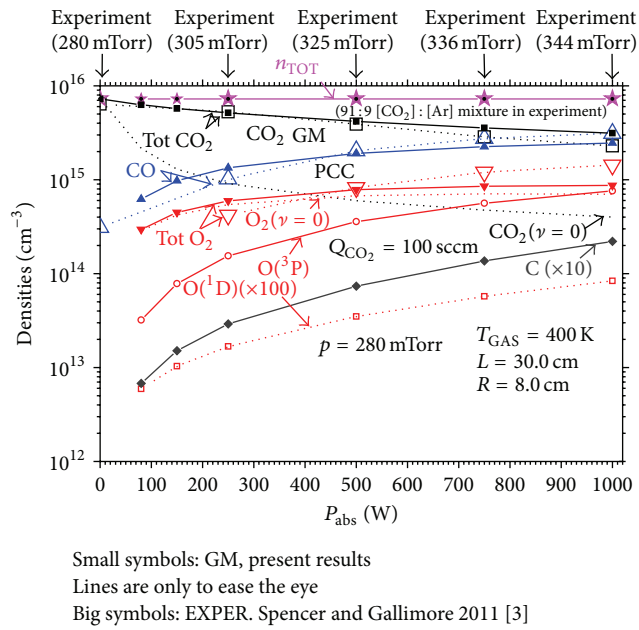

FIGURE 12: PCC for conditions similar to those of Figure 9 but for 100 sccm feeding; Tot stands for total and EXPER for experiment.

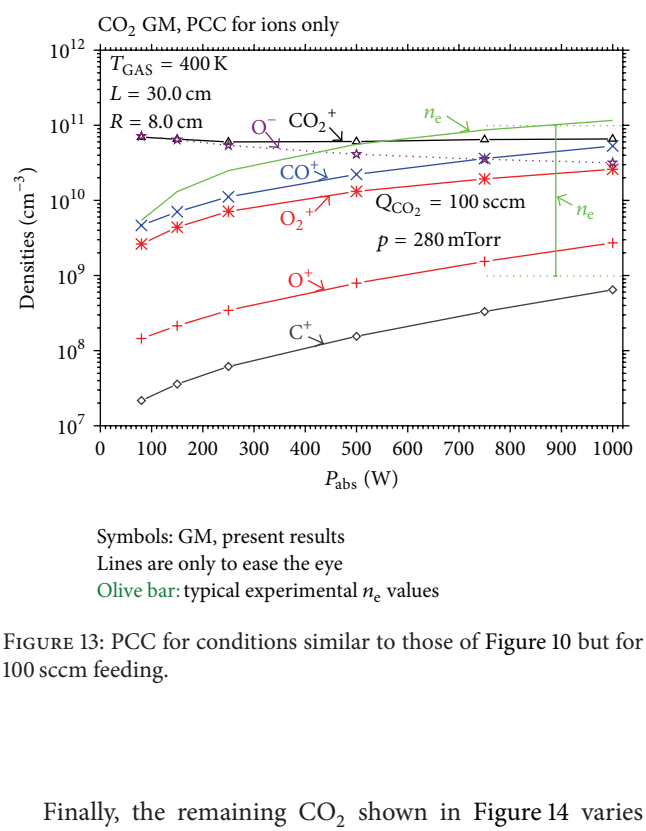

FIGURE 13: PCC for conditions similar to those of Figure 10 but for 100 sccm feeding.

the molecular ones (up to two orders of magnitude). For 1 kW, densities of C^+ and of $O_2{}^+$ become the same as this of $CO_2{}^+$. As expected, n_e is increasing with the absorbed power, reaching quite higher values than those which are commonly encountered for $P_{abs} < 500$ W. Important results concerning the remaining CO_2 percentage in the discharge and the electronegativity (empty stars) are illustrated in Figure 11, together with T_e values shown by the red line joining squares.

Both remaining CO_2 (full black squares) and electronegativity α (empty stars) are fast diminishing with increasing absorbed power and in rather similar way. In Figure 11, calculated T_e values noted by red squares are also illustrated. They have rather low values and vary very little. Inversely, the ξ_{TOT} values represented by the blue line although increasing with P_{abs} they remain clearly very small; hence, they are shown multiplied by a factor of 10^3.

Results obtained for a higher feeding of $Q_{CO_2} = 100$ sccm and for 280 mTorr pressure are illustrated in Figures 12, 13, and 14 in a similar way with Figures 9, 10, and 11 correspondingly. Typical Q_{CO_2} and p values have been selected in order to ease the comparison with the available experiment of [3].

Comparing the PCCs shown in Figures 9 and 12 we see that CO density never reaches the CO_2 density values illustrated in the second figure. This fact was expected, as the feeding is significantly higher while the absorbed power remains the same. The ionic components shown in Figure 13 present a quite bigger difference between O^+ and C^+ densities than this shown in Figure 10 for the same ions, suggesting that for large feedings O atoms are ionized preferably than C ones.

Finally, the remaining CO_2 shown in Figure 14 varies much slower than in the low fed discharge of Figure 11, as the absorbed powers are not sufficient to dissociate the CO_2 in case of abundant feeding. Electronegativity α (empty stars) is here much higher than in the case shown in the analogous Figure 11 and ionization percentage ξ_{TOT} (blue line) is an order of magnitude smaller.

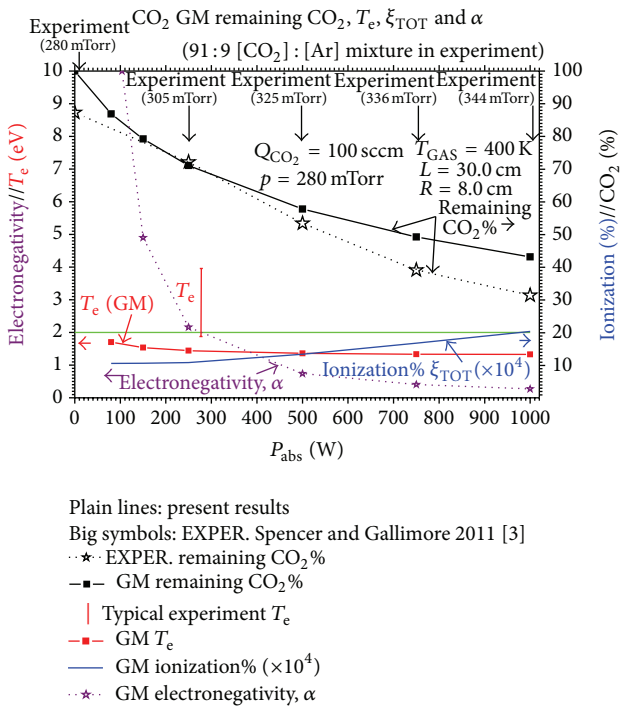

Figure 14: Remaining CO_2, T_e, ξ_{TOT}, and α as a function of the absorbed power P_{abs} for 100 sccm feeding; EXPER stands for experiment.

4. Experimental Results from a Radiofrequency Discharge Compared with CO_2 GM Calculations

In the following we compare experimental results from the Cathode Test Facility at the Plasmadynamics and Electric Propulsion Laboratory (PEPL) of the University of Michigan, Ill, published in [3], with the corresponding theoretical results of our model. In this experiment, a radiofrequency plasma discharge constituted by a cylinder of length of about 30 cm (approximate value taken from the Figure 1 diagram of [3]) and of radius 7.5 cm ends in a chamber of 244 cm of length and of 61 cm of diameter. It is powered by 1 kW radiofrequency double helix antenna supply of 13.56 MHz. Although Cathode Test Facility was mainly fed by CO_2, additional Ar feeding was also provided, results of which we consider of minor importance for the moment; we address this subject later on. Details on the facility and results on CO_2 dissociation in radiofrequency discharges are given in [3] and references therein. Specifically, experimental results addressed here are taken from Figures 2(a) and 2(b) of [3]. They have been included in Figures 3 to 14 of the previous section, noted by big symbols and by the mentioned "experiment". Full pink stars are used for n_{TOT} and triangles, squares, and inverse triangles are used for CO, Tot CO_2, and Tot O_2 densities correspondingly.

Figures 3 to 5 and Figures 6 to 8 compare pressure depending results and Figures 9 to 11 and Figures 12 to 14 power depending ones for the previously chosen cases of 15 sccm low feeding and of 100 sccm high feeding correspondingly. A pressure around 80 mTorr has been chosen for the low feeding of 15 sccm case and a higher pressure of around 280 mTorr and more for the high feeding of 100 sccm. Note that typical form factors selected for our calculations which are shown in the figures are very near to those pertaining to the experiment. Double values are occasionally indicated for the experiment, because of small discrepancy in theory-experiment pressures. In any case, the two values indicated for Q_{CO_2} = 15 sccm feeding are always very close. In Figure 3 the total theoretical density n_{TOT} varies with a slope of p/k_BT_{GAS}. We used our theoretical values of n_{TOT} to obtain approximate absolute values of the densities corresponding to the experiment, as only the values of the exhausting flow rates are provided in [3]. For P_{abs} = 250 W, theoretical total CO_2 (Tot CO_2) and CO values are in very good agreement with experimental ones, with total O_2 (Tot O_2) values slightly higher than the experiment. Ion densities, being significantly lower, have not been measured; therefore, no comparison is possible for the theoretical results shown in Figures 4 and 7. The vertical green bar shows typical n_e values reported in [3] with the green curve giving theoretical n_e values. These are in agreement in the case of Figures 3 and 4 with the commonly expected values mentioned in [3]. Figure 5 gives theoretical values obtained for the remaining CO_2 percentage which are slightly lower than the experimental ones for a pressure slightly less than 100 mTorr.

Figure 6, which pertains to a feed of Q_{CO_2} = 100 sccm for the same absorbed power of 250 W, shows the experimental n_{TOT} identified to the theoretical one, the latter varying according to the same slope of p/k_BT_{GAS} given in the Figure 3 case. Experimental values of Tot CO_2 in pressures about 300 mTorr are in total agreement with the theory, while the latter gives CO and O_2 densities values slightly higher than the experiment. Calculated electron densities n_e are within 10^{11}–10^9 cm^{-3}, as expected. The calculated remaining CO_2 percentage in this case is in very good agreement with the experiment, while T_e values are rather low. It is to be noted that we have made an approximate evaluation of the remaining CO_2 when following the experiment. The experimental values of the remaining CO_2 percentage, appearing in the figures (namely, Figures 5, 8, 11, and 14), have been calculated by us without taking into account the other plasma constituents and notably the atomic oxygen O(^{3}P) which, according to our calculations, is present in a considerable amount. Reference of its presence was made in [3]. Hence, the experimental values to be compared with our calculations should be slightly smaller if the O(^{3}P) presence was taken into account. For a more accurate calculation of the remaining CO_2 percentage, see Table 5 in the following. Inspection of Figure 8 shows a very good agreement of theory with experiment for the remaining CO_2 percentage for a pressure about 300 mTorr. However, theoretical T_e values are quite lower (about half) than those expected (red vertical bar) in this pressure region.

Variations of the theoretical plasma component densities of the PCC for 15 sccm shown in Figure 9 compare rather favorably with the experimental data. However, it has to be noted that, although this PCC refers to 80 mTorr pressure,

the compared experimental pressure values are in fact slowly increasing with the absorbed power, going up to 103 mTorr for 1 kW. Also, the calculated electron density is rather higher than the typical one for high P_{abs}.

For a low feeding of $Q_{CO_2} = 15$ sccm, Figure 11 shows theoretical values of the remaining CO_2 percentage near to the experimental ones, but theoretical T_e values are again about half than those often observed experimentally, which are illustrated by the red vertical bar.

Results of our calculations for a feeding of 100 sccm and a higher pressure of 280 mTorr (with the experimental ones going up to 344 mTorr) are illustrated in Figure 12 for neutral species. Note that no comparison with our theoretical results illustrated in Figure 13 was possible as was also the case with the 15 sccm feeding (Figure 10), experimental ionized species densities being not measured in [3]. Inspection of Figure 12 shows that our theoretical results for neutral species are in satisfactory agreement with the experiment. This is not the case with the remaining CO_2 percentage corresponding to high absorbed power values shown in Figure 14, where our calculations show a remaining CO_2 percentage as high as 43% for 1 kW absorbed power, while the experimental value is about 31%. Otherwise, the generally small discrepancies observed will be now reconsidered following a detailed evaluation of the influence of the mixing with Ar. In doing so, we elaborated Table 5 illustrating the change of the results in comparison which is due to the Ar presence.

Table 5 shows species percentages calculated from the ratios of exhausting flow rate for the experiment. It provides a first comparison of the results obtained by our model for pure CO_2, for pure Ar and for a CO_2/Ar mixture of about $[CO_2]:[Ar]$ 60 : 40 corresponding approximately to the experiment (indicated by †). Our theoretical results for the corresponding feedings (column Q_{TOT}) are given in four rows (indicated by ††). The last one of the four gives the results obtained by a separate GM meant for a mixture of CO_2 and Ar. The differences between CO_2 plasma results pertaining to 15 sccm and 25 sccm are in general small, except for the $n_C/(n_{TOT} - n_{Ar})$ ratio case. For the Ar plasma a previously available GM [10] has been used, giving much higher n_e and n_+ values (n_+ represents the total density of positive ions), because there is no energy spent in chemistry processes in the Ar case. Then, for the $[CO_2]:[Ar]$ mixture calculations only the n_+ and n_e densities change considerably, but these have not been measured in any case. For the latter, calculated values are particularly high. Values shown in the last row, adapted to the mixture with Ar, are those to be retained for comparison, instead of those of the first row. This small change leads to more satisfactory values for the theory-experiment comparison.

5. Electric Propulsion Applications of CO_2 Discharges Global Modeling

GMs have been lately used to support the EP technology, when Ar [10], N_2O and N_2/O_2 mixtures [38] are used as propellants. Details are available in [2]. Given the type and the form factor of the thruster and the composition of the propellant, GMs provide important information which can be contained in diagrams as follows.

(i) Functioning diagram (FD) which is composed of iso-T_e and iso-P_{abs} curves defining the ionization percentage of the plasma as a function of the pressure.

(ii) Plasma components composition (PCC) diagram which contains the curves giving the density variation of each component of the plasma, also as a function of the pressure.

FD and PCC diagrams are on the basis of the thruster modeling, also allowing for optimization, monitoring and evaluation of the erosion of the propellant facing surfaces, through nonperturbing optical emission spectroscopy diagnostics [39, 40]. It is evident that optical emission spectroscopy has to be adapted to the type and to the form factor of the device. When the propellant has a varying composition, as is the case with air-breathing technology, FD and PCC diagrams become of paramount importance [41] because changes of the N_2/O_2 percentage lead to discharges with quite different characteristics. A typical application of our CO_2 GM is the technical support for CO_2 breathing thrusters, which are expected to be used in low and very low trajectory devices meant to work, for example, in the Martian atmosphere environment, where the atmospheric density is significantly lower than this of the Earth for the same altitude.

In the present work, we address only three typical cases of our CO_2 GM application in EP, namely, a low pressure case for a thruster functioning with a low feeding rate (Section 5.1) and with a high feeding one (Section 5.2) and also a case of higher pressure, for a thruster functioning under high feeding (Section 5.3). As was the case with previous calculations aiming at helicon thruster modeling, the Landau damping approximation has been used in the first two cases [10]; this approximation allows for considerable simplification of the calculations. However, in the third case, where the expected n_e is low and the pressure rather high; this approximation is not applicable and was not used.

5.1. Low Pressure, Low Feeding Devices. We consider here a small helicon type thruster of a length of $L = 13$ cm and of core radius $R_C = 0.3$ cm. The CO_2 feeding is of 20 sccm and the pressure varies from 3 mTorr to 10 mTorr. Results of the GM for this case are shown in Figure 15, giving the applicable FD when the absorbed power varies from 50 W to 1000 W.

Depending on the pressure, the considered P_{abs} values allow for T_e values from 5 eV up to 60 eV. The thick arrow corresponds to $P_{abs} = 200$ W; its slope indicates how handy is the plasma ionization in this case. The concomitant PCC of Figure 16 shows the corresponding densities of the plasma constituents for $P_{abs} = 200$ W.

Although Figure 16 is somewhat analogous to Figures 3 and 6, because of the high absorbed power in a small volume the ionic species and n_e become here much higher. CO_2^+ (black empty triangles) is the most abundant species for low pressures, replaced by O^+ (red crosses) for the higher ones. The most abundant neutral species are successively $O(^3P)$ (red empty squares) and CO (full blue triangles). As is the

Table 5: Results obtained taking into account the presence of Ar in the discharge. Conditions: $p = 80$ mTorr; $P_{abs} = 250$ W; $T_{GAS} = 400$ K; approximate form factor $L = 30$ cm; $R = 8$ cm.

Discharge case	Q_{tot} (sccm)	T_e (eV)	n_e (∗)	O^- (∗)	n_+ (∗)	Ratio $n_{CO_2}/(n_{TOT} - n_{Ar})$	Ratio $n_{CO}/(n_{TOT} - n_{Ar})$	Ratio $n_{O_2}/(n_{TOT} - n_{Ar})$	Ratio $n_O/(n_{TOT} - n_{Ar})$	Ratio $n_C/(n_{TOT} - n_{Ar})$	Ratio n_{Ar}/n_{TOT}
Experiment $[CO_2]:[Ar]$ 60 : 40	**25 (15 + 10)**†					**44.4**†	**44.4**†	**11.1**†			**35.7**†
GM CO_2	**15**††	**1.568**††	**5.49**††	**4.28**††	**9.77**††	**38.1**††	**38.7**††	**17.4**††	**5.1**††	**0.6**††	
GM CO_2	**25**††	**1.600**††	**5.21**††	**5.28**††	**10.49**††	**48.1**††	**32.7**††	**14.5**††	**4.4**††	**0.3**††	
GM Ar	**25**††	**1.467**††	**156.9**††		**156.9**††						**100**††
GM $[CO_2]:[Ar]$ 60 : 40	**25 (15 + 10)**††	**1.537**††	**8.42**††	**4.41**††	**12.83**††	**38.8**††	**37.8**††	**16.1**††	**6.8**††	**0.6**††	**33.6**††
Experiment $[CO_2]:[Ar]$ 60 : 40	**25 (15 + 10)**†					**41.1**†	**41.1**†	**10.3**†	**6.8**$^{\triangle}$	**0.6**$^{\triangle}$	**34.0**†

Experimental density ratios (given in percentage) calculated from the flow of species created in the discharge measured in [3] with help of the present theoretical results.
n_O and n_C percentage (indicated by △) are evaluated assuming 7.4% of the sum of C + O percentages.
(∗) densities in 10^{10} cm^{-3}.

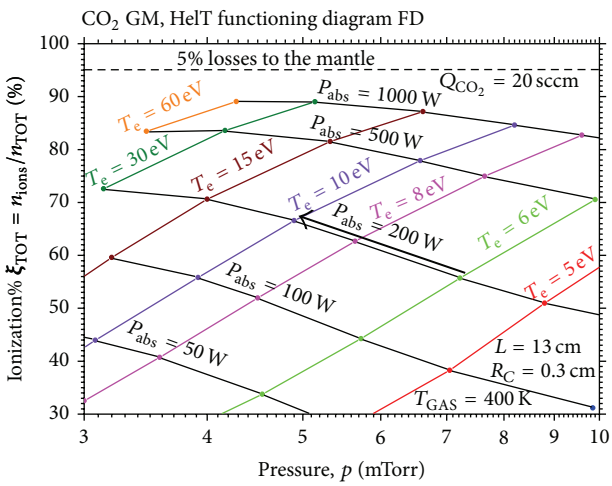

FIGURE 15: FD for a 20 sccm CO_2 fed HelT.

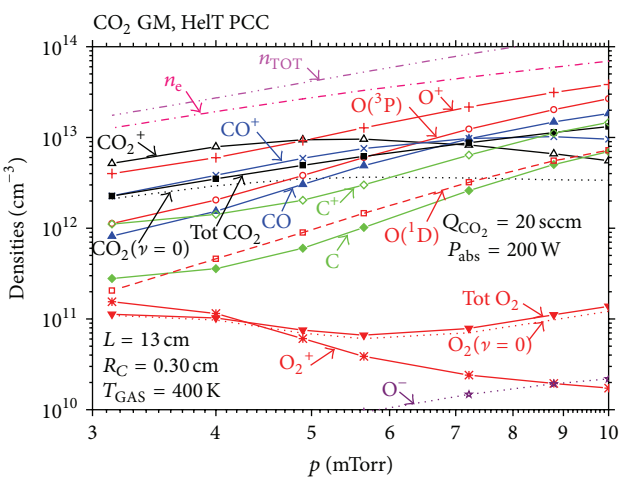

FIGURE 16: PCC for a 20 sccm CO_2 fed HelT; Tot stands for total.

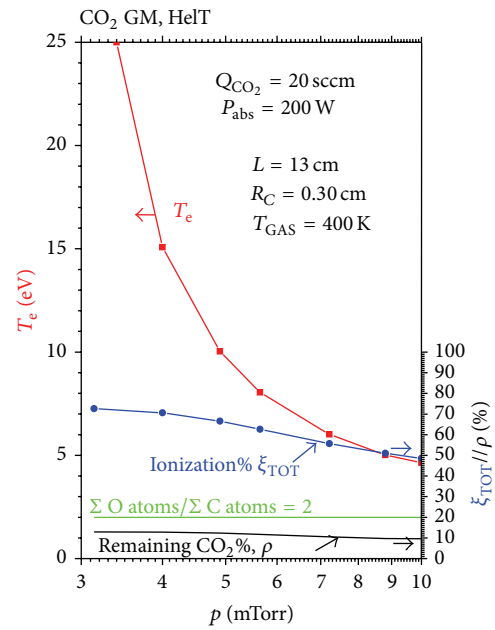

FIGURE 17: Remaining CO_2, T_e, and ξ_{TOT} for a 20 sccm CO_2 fed HelT.

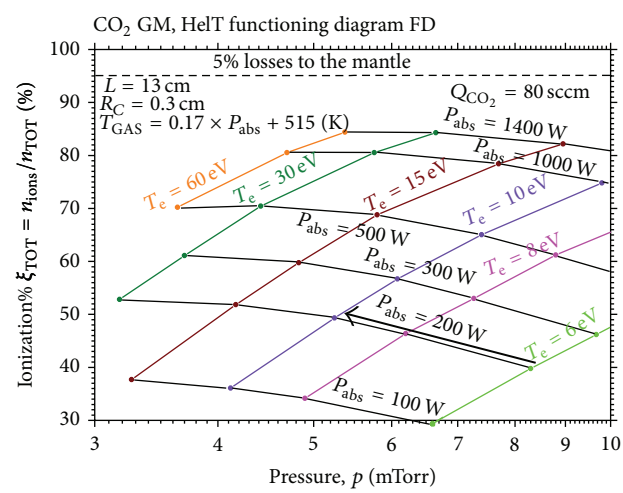

FIGURE 18: FD for 80 sccm CO_2 fed HelT.

case for the ions, abundance of Tot CO_2 (black squares), although being the most important for low pressures, is exceeded by $O(^3P)$ and CO abundances for higher ones. The temperature of the gas is taken as $T_{GAS} = 400$ K. Figure 17 shows in this case the considerably high T_e (red squares) for small pressure values and the total ionization parameter ξ_{TOT} (blue circles, values to be read at the right side of the figure) which vary from 70% to 50% approximately. The indicated remaining CO_2 percentage ρ stays very small, about 10% only.

5.2. Low Pressure, High Feeding Devices. It is evident that whenever we aim to investigate a situation analogous to this reported in Section 5.1 but with a higher CO_2 feeding, typically of 80 sccm instead of 20 sccm, the characteristics of the discharge are quite different. Practically, such an increase of the feeding should not be a problem in case of "*in situ*" availability of the propellant even if the ionization percentage remains low. Figure 18 shows the corresponding FD for the same pressures with those of Figure 15 but for higher feeding. However, higher P_{abs} lines are added in this case, in order to obtain results in a sufficiently high ionization region. Because of the inclusion of increased P_{abs} values, the T_{GAS} has been considered here as varying, according to the formula $T_{GAS} = 0.17 \cdot P_{abs} + 515$, with T_{GAS} in K and P_{abs} in W units. This formula is based on the formula given in [11] which was conveniently shifted to reach a gas temperature $T_{GAS} = 600$ K when $P_{abs} = 500$ W. Comparing the FDs belonging to 20 sccm and to 80 sccm, we see that with increasing feeding the ionization becomes more difficult for the same P_{abs}. This is manifested by the slope of the thick arrow, also present in Figure 18. It illustrates the previously observed fact [2] that optimization of the feeding is an important part of the thruster study.

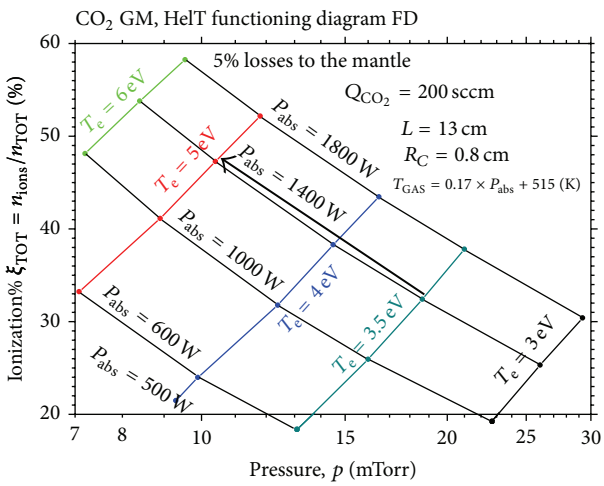

FIGURE 19: FD for a 200 sccm CO_2 fed HelT.

5.3. High Pressure, High Feeding Devices. Another interesting case is encountered when both the pressure and the feeding are quite high. Such a case could be considered, for example, when the thruster environment is in a quite high pressure and of course when the propellant is abundant. Innovating types of EP could be devised in such cases, possibly using mixtures as propellants in order to increase the ionization and hence the thrust. Figure 19 shows a FD corresponding to such a case.

Although the length $L = 13$ cm was kept the same, we address here a larger device, with $R_C = 0.8$ cm. Because of the large feeding rate selected ($Q_{CO_2} = 200$ sccm), we are interested in higher pressure values and we seek higher P_{abs} values, going up to 1800 W for a pressure of about 10 mTorr in order to approach 60% of ionization. Figure 20 shows a PCC diagram concomitant to the FD of Figure 19 in case of 1400 W of P_{abs}. For a pressure doubling to go from 10 mTorr to 20 mTorr, the total density n_{TOT} is also about doubling and the n_e increases rather slower from $4.5 \cdot 10^{13}$ to $7 \cdot 10^{13}$ cm^{-3}. Densities of O(^{3}P), CO, and CO_2 are similar and slightly exceeded by the most abundant ion O^+. O_2 and O^- densities are much smaller than those of O(^{3}P), CO and CO_2 and O_2^+ almost absent.

Figure 21 shows concomitant variations of T_e, of ionization and of remaining CO_2 percentage for the conditions corresponding in the previous Figure 20. The latter never exceeds 20%, even for a high pressure of 20 mTorr. The total ionization percentage diminishes roughly from 50% to 30% with increasing pressure, which indicates that an abundant *in situ* source of CO_2 has to be available in order to consider CO_2 as EP propellant under such conditions. The electron temperature falls for increasing pressures, in a similar way in this case to the ionization percentage.

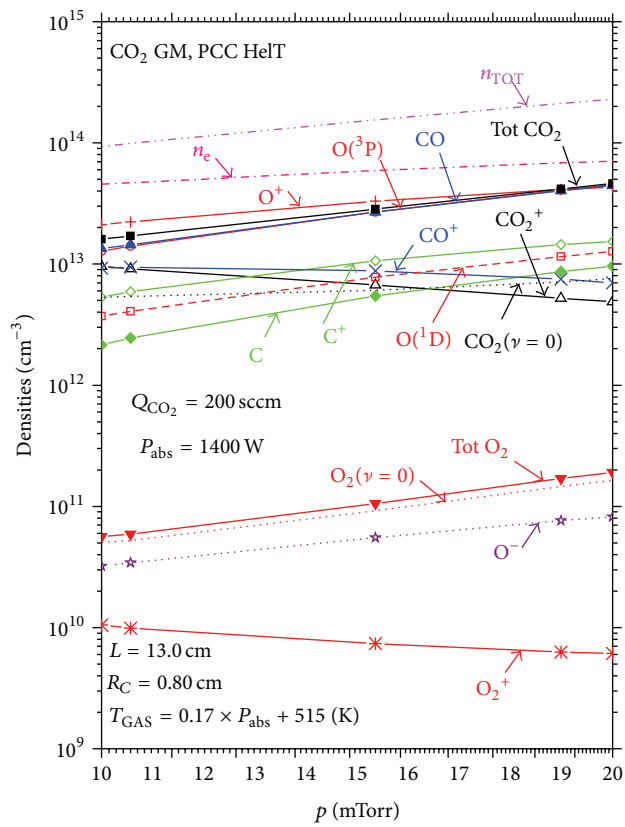

FIGURE 20: PCC for a 200 sccm CO_2 fed HelT; Tot stands for total.

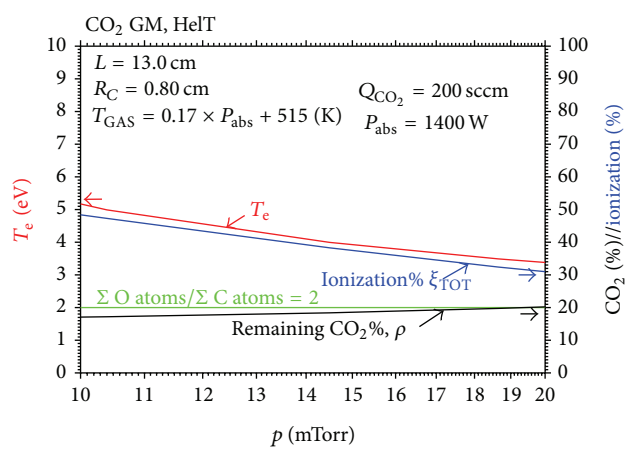

FIGURE 21: Remaining CO_2, T_e, and ξ_{TOT} for a 200 sccm CO_2 fed HelT.

6. Conclusions

A systematic exploitation of our GM devoted to CO_2 discharges allowed for description of the latter in various typical conditions. Applications of interest to radiofrequency type plasma reactors and CO_2 atmospheres and to EP technology have been separately addressed according to their specificity. For the first applications, available experimental data [3] allowed for theory-experiment comparison, with satisfactory results leading to a first validation of our model. For the second type of applications, FD and PCC analysis allowed for developing a basis for study, optimization, and diagnostics of plasma thrusters when they are fed with CO_2. Because of lack of dedicated experimental devices, no validation has been possible for the moment concerning plasma thruster devices.

We are looking forward to finding experimental facilities which will help us to do so. In all, the present model was able to provide satisfactory characterization of various cases of CO_2 plasmas.

For low ionized plasmas, the interrelation of dimensions, feeding, absorbed power, pressure, ionization percentage, electron density, and temperature has been investigated. In case of plasmas exhibiting higher ionization degree, pertaining to lower pressure and considerable absorbed power values, characteristics concerning electric plasma thrusters have been systematically studied and summarized using standard FD and PCC diagrams. These are presented for selected plasma conditions. Low and high pressure conditions have been addressed separately and the need for higher absorbed power in the second case in order to reach satisfactory ionization levels has been again illustrated. It is evident that adequate experimental facilities are needed to obtain a better insight on CO_2 plasmas of interest to electric propulsion, a development to which our CO_2 model is meant to contribute substantially.

The presented diagrams can be used for modeling of discharges in CO_2 atmospheres, including mixtures with other gases, reacting or inert, present in aerospace environments. These have a significant potential for industrial applications, for example, to reduce unwanted CO_2 abundance [3] and extract usable oxygen. They are also meant for use in EP when CO_2 is used as propellant in various propulsion devices, also in case of feeding by gas mixtures. In fact, as was shown through the elaboration of Table 5, the present model can be extended in order to obtain modeling of gases mixtures, whenever the corresponding GMs are already available. This allows for straightforward study of CO_2, N_2, and O_2 mixtures discharges of current interest to industrial applications [5, 42].

Nomenclature

D_j: Neutral diffusion coefficient, $D_j = (k_B T_{GAS} \lambda_j)/(v_j M_{CO_2})$
DISS: Dissociation
DXW, j: Deexcitation on the wall for a species j
E_{IONIZ}: Ionization energy
ELAS: Elastic
EP: Electric Propulsion
EXC: Excitation
FD: Functioning Diagram
GL: Ground Level
GM: Global Model
h_L: Axial edge to center ratio of positive ion density
h_R: Radial edge to center ratio of positive ion density
HelT: Helicon thruster
IONIZ: Ionization
ICP: Inductively Coupled Plasma
j: Species state(s)
k_B: Boltzmann constant, $k_B = 1.3807 \cdot 10^{-23}\ \mathrm{J{\cdot}K^{-1}}$
k_j: Processes rate coefficient involving state j
L: Plasma length
M_{CO_2}: CO_2 mass
n_e: Electron density
n_+: Total density of positive ions
n_{TOT}: Total plasma species density
p: Pressure
P_{abs}: Absorbed power
PCC: Plasma Components Composition
R: Plasma radius
R_C: Radius of the plasma core
RW, X^+: Recombination on the wall for X^+ species
T_e: Electron temperature
T_{GAS}: Gas temperature
u_B: Bohm velocity, $u_B = (eT_e/M)^{1/2}$
V: Discharge volume
$\varepsilon, \varepsilon_{C,X}$: Collisional energy loss of the electrons, colliding with species X
v_j: Neutral mean velocity, $v_j = (8k_B T_{GAS}/\pi M_X)^{1/2}$
γ_j: Sticking coefficient for the neutral species j on the wall surface
ξ_{TOT}: Total ionization percentage
ρ: Remaining CO_2 percentage
$\sigma_{j,X}$: Cross section pertaining to state j with species X.

Conflict of Interests

The authors declare that there is no conflict of interests regarding the publication of this paper.

References

[1] A. Lieberman and A. J. Lichtenberg, *Principles of Plasma Discharges and Materials Processing*, John Wiley & Sons, Hoboken, NJ, USA, 2nd edition, 2005.

[2] K. Katsonis and C. Berenguer, *Global Modeling of N_2O, Air and N_2 Discharges and Applications*, Lambert Academic Publishing, Saarbrücken, Germany, 2013.

[3] L. F. Spencer and A. D. Gallimore, "Efficiency of CO_2 dissociation in a radio-frequency discharge," *Plasma Chemistry and Plasma Processing*, vol. 31, no. 1, pp. 79–89, 2011.

[4] J. L. Fox, "CO_2^+ dissociative recombination: a source of thermal and nonthermal C on Mars," *Journal of Geophysical Research A: Space Physics*, vol. 109, no. 8, Article ID A08306, 2004.

[5] P. Noeding, *Review of Physico-Chemical CO_2 Modelling and Recommendation for Improvement*, SACOMAR: Technologies for Safe and Controlled Martian Entry Project, 2011.

[6] National Geographic, *Beyond Our Galaxy: Exploring The Vastness of Space*, National Geographic, Washington, DC, USA, 2014.

[7] C. Arpigny, "The resonance-fluorescence excitation of the CO^+ comet-tail bands of Comet Humason (1961e)," *Annales d'Astrophysique*, vol. 27, p. 406, 1964.

[8] C. Berenguer and K. Katsonis, "Modeling and diagnostics of H/He mixture high temperature space plasmas," in *Proceedings of the ESA 5th International Workshop Radiation of High Temperature Gases in Atmospheric Entry*, Barcelona, Spain, October 2012.

[9] K. Katsonis and C. Berenguer, "A complete global model for He torch experiments and atmospheric entry study," in *Proceedings of the 5th International Workshop on Radiation of*

High Temperature Gases in Atmospheric Entry, Barcelona, Spain, October 2012.

[10] C. Berenguer and K. Katsonis, "Plasma reactors and plasma thrusters modeling by Ar complete global models," *International Journal of Aerospace Engineering*, vol. 2012, Article ID 740869, 18 pages, 2012.

[11] E. G. Thorsteinsson and J. T. Gudmundsson, "A global (volume averaged) model of a nitrogen discharge: I. Steady state," *Plasma Sources Science and Technology*, vol. 18, no. 4, Article ID 045001, 2009.

[12] K. Katsonis and C. Berenguer, "Global modeling of N_2O discharges: rate coefficients and comparison with ICP and glow discharges results," *International Journal of Aerospace Engineering*, vol. 2013, Article ID 737463, 25 pages, 2013.

[13] C. Lee and M. A. Lieberman, "Global model of Ar, O_2, Cl_2, and Ar/O_2 high-density plasma discharges," *Journal of Vacuum Science & Technology A*, vol. 13, no. 2, pp. 368–380, 1995.

[14] S. Kim, M. A. Lieberman, A. J. Lichtenberg, and J. T. Gudmundsson, "Improved volume-averaged model for steady and pulsed-power electronegative discharges," *Journal of Vacuum Science & Technology A*, vol. 24, no. 6, pp. 2025–2040, 2006.

[15] M.-T. Lee and V. McKoy, "Cross sections for electron impact excitation of the low-lying electron states of CO_2," *Journal of Physics B: Atomic and Molecular Physics*, vol. 16, no. 4, pp. 657–669, 1983.

[16] Y. Itikawa, "Cross sections for electron collisions with carbon dioxide," *Journal of Physical and Chemical Reference Data*, vol. 31, no. 3, pp. 749–767, 2002.

[17] P. Laborie, J.-M. Rocard, and J. A. Rees, *Electronic Cross-Sections and Macroscopic Coefficients. 2—Metalic Vapours and Molecular Gases*, Dunod, Paris, France, 1971.

[18] Y. Nakamura, "Drift velocity and longitudinal diffusion coefficient of electrons in CO_2/Ar mixtures and electron collision cross sections for CO_2 molecules," *Australian Journal of Physics*, vol. 48, p. 357, 1995.

[19] M. Kitajima, S. Watanabe, H. Tanaka, M. Takekawa, M. Kimura, and Y. Itikawa, "Differential cross sections for vibrational excitation of CO_2 by 1.5–30 eV electrons," *Journal of Physics B*, vol. 34, no. 10, pp. 1929–1940, 2001.

[20] K.-H. Kochem, W. Sohn, N. Hebel, K. Jung, and H. Ehrhardt, "Elastic electron scattering and vibrational excitation of CO_2 in the threshold energy region," *Journal of Physics B: Atomic and Molecular Physics*, vol. 18, no. 22, pp. 4455–4467, 1985.

[21] H. Nakatsuji, "Cluster expansion of the wavefunction, valence and rydberg excitations, ionizations, and inner-valence ionizations of CO_2 and N_2O studied by the sac and sac CI theories," *Chemical Physics*, vol. 75, no. 3, pp. 425–441, 1983.

[22] A. V. Phelps, "Cross sections and swarm coefficients for nitrogen ions and neutrals in N_2 and argon ions and neutrals in Ar for energies from 0.1 eV to 10 keV," *Journal of Physical and Chemical Reference Data*, vol. 20, p. 557, 1991.

[23] K. Orimi, S. Watanabe, H. Kohguchi, and K. Yamasaki, "Direct determination of the rate coefficient for the reaction of $O(^1D)$ with OCS," *Chemical Physics Letters*, vol. 483, no. 1–3, pp. 16–20, 2009.

[24] B. G. Lindsay and M. A. Mangan, "Cross sections for ion production by electron collisions with molecules," in *Photon and Electron Interactions with Atoms, Molecules and Ions*, vol. I/17C, pp. 5001–5077, Landolt-Börnstein, Springer, Berlin, Germany, 2003.

[25] L. R. LeClair and J. W. McConkey, "On $O(^1S)$ and $CO(a^3\pi)$ production from electron impact dissociation of CO_2," *Journal of Physics B*, vol. 27, no. 17, pp. 4039–4055, 1994.

[26] D. Rapp and D. D. Briglia, "Total cross sections for ionization and attachment in gases by electron impact. II. Negative-ion formation," *The Journal of Chemical Physics*, vol. 43, no. 5, pp. 1480–1489, 1965.

[27] K. Seiersen, A. Al-Khalili, O. Heber et al., "Dissociative recombination of the cation and dication of CO_2," *Physical Review A*, vol. 68, no. 2, Article ID 022708, 2003.

[28] A. J. Sedlacek, D. R. Harding, R. E. Weston Jr., T. G. Kreutz, and G. W. Flynn, "Probing the $O(^1D)+CO_2$ reaction with second-derivative modulated diode laser spectroscopy," *The Journal of Chemical Physics*, vol. 91, no. 12, pp. 7550–7556, 1989.

[29] K. Katsonis, C. Berenguer, A. Kaminska, and M. Dudeck, "Argon 4s and 4p excited states atomic data applied in ARC-JET modeling," *International Journal of Aerospace Engineering*, vol. 2011, Article ID 896836, 15 pages, 2011.

[30] H. Singh, J. W. Coburn, and D. B. Graves, "Recombination coefficients of O and N radicals on stainless steel," *Journal of Applied Physics*, vol. 88, no. 6, pp. 3748–3755, 2000.

[31] R. Schunk and A. Nagy, *Ionospheres: Physics, Plasma Physics, and Chemistry*, Cambridge University Press, New York, NY, USA, 2000.

[32] C. S. Corr, S. Gomez, and W. G. Graham, "Discharge kinetics of inductively coupled oxygen plasmas: experiment and model," *Plasma Sources Science and Technology*, vol. 21, no. 5, Article ID 055024, 2012.

[33] J. T. Gudmundsson, I. G. Kouznetsov, K. K. Patel, and M. A. Lieberman, "Electronegativity of low-pressure high-density oxygen discharges," *Journal of Physics D: Applied Physics*, vol. 34, no. 7, pp. 1100–1109, 2001.

[34] Y.-K. Kim and J.-P. Desclaux, "Ionization of carbon, nitrogen, and oxygen by electron impact," *Physical Review A*, vol. 66, no. 1, Article ID 012708, 2002.

[35] M. Allan, "Electron collisions with CO: elastic and vibrational excitation cross sections," *Physical Review A: Atomic, Molecular, and Optical Physics*, vol. 81, no. 4, Article ID 042706, 2010.

[36] M. M. Ristić, G. B. Poparić, and D. S. Belić, "Electron impact excitation of the a3Π state of CO: full range differential cross sections," *Publications de l'Observatoire Astronomique de Beograd*, vol. 89, pp. 41–44, 2010.

[37] G. B. Poparić, "Resonant excitation of molecules by low-energy electrons," *Facta Universitatis—Series: Physics, Chemistry and Technology*, vol. 6, p. 41, 2008.

[38] K. Katsonis and C. Berenguer, "Global modeling of N_2O discharges: helicon plasma thruster application," *International Journal of Aerospace Engineering*, vol. 2013, Article ID 467503, 9 pages, 2013.

[39] C. Berenguer, K. Katsonis, and D. Pavarin, "The resonant lines VUV transitions in rare gas plasma thrusters," in *Proceedings of the 32nd International Electric Propulsion Conference (IEPC '11)*, Wiesbaden, Germany, September 2011, IEPC-2011-170.

[40] K. Katsonis, C. Berenguer, D. Pavarin et al., "Optical diagnostics of a low temperature argon thruster," in *Proceedings of the 32nd International Electric Propulsion Conference (IEPC '11)*, IEPC-2011-169, Wiesbaden, Germany, September 2011.

[41] K. Katsonis and C. Berenguer, "A set of functioning diagrams and plasma components compositions for air breathing thrusters modeling and diagnostics," Tech. Rep. DEDALOS 2014-01, 2014.

[42] N. L. Aleksandrov, S. V. Kindysheva, I. N. Kosarev, and A. Y. Starikovskii, "Plasma decay in air and $N_2 : O_2 : CO_2$ mixtures at elevated gas temperatures," in *Proceedings of the 47th AIAA Aerospace Sciences Meeting including the New Horizons Forum and Aerospace Exposition*, Orlando, Fla, USA, January 2009.